HHS Public Access

Author manuscript

Eur J Pharm Sci. Author manuscript; available in PMC 2025 June 08.

Published in final edited form as:

Eur J Pharm Sci. 2025 June 01; 209: 107093. doi:10.1016/j.ejps.2025.107093.

Assessment of ventilation heterogeneity and particle deposition in asthmatics using combined SPECT/CT imaging and computational modeling approaches

Xuan Zhang[a,b], **Prathish K. Rajaraman**[a,b], **Frank Li**[a,c], **Sanghun Choi**[d], **Alejandro P. Comellas**[e], **Eric A. Hoffman**[f,c], **Sean B. Fain**[f,c,g,h], **David W. Kaczka**[i,c], **Benjamin M. Smith**[j,k], **Jiwoong Choi**[l], **Mario Castro**[l], **Sally E. Wenzel**[m], **Nizar N. Jarjour**[n], **Mark L. Schiebler**[n], **Elliot Israel**[o], **Bruce D. Levy**[o], **John V. Fahy**[p], **Serpil C. Erzurum**[q], **Andrew Babiskin**[r], **Minori Kinjo**[s], **Ross Walenga**[s], **Ching-Long Lin**[a,b,c,f,*]

[a]IIHR-Hydroscience & Engineering, University of Iowa, Iowa City, IA, USA

[b]Department of Mechanical Engineering, University of Iowa, Iowa City, IA, USA

[c]Roy J. Carver Department of Biomedical Engineering, University of Iowa, Iowa City, IA, USA

[d]School of Mechanical Engineering, Kyungpook National University, Daegu, South Korea

[e]Department of Internal Medicine, University of Iowa, Iowa City, IA, USA

[f]Department of Radiology, University of Iowa, Iowa City, IA, USA

[g]Department of Electrical and Computer Engineering, University of Iowa, Iowa City, IA, USA

[h]Department of Health and Human Physiology, University of Iowa, Iowa City, IA, USA

[i]Departments of Anesthesia and Radiology, University of Iowa, Iowa City, IA, USA

[j]Department of Medicine, College of Physicians and Surgeons, Columbia University, New York, NY, USA

[*]Corresponding author at: IIHR-Hydroscience & Engineering, University of Iowa, Iowa City, IA, USA. ching-long-lin@uiowa.edu (C.-L. Lin).

Disclosure

The following companies provided financial support for study activities at the Coordinating and Clinical Centers beyond the third year of patient follow-up: AstraZeneca, Boehringer-Ingelheim, Genentech, GlaxoSmithKline, Sanofi–Genzyme–Regeneron, and TEVA. These companies had no role in study design or data analysis, and the only restriction on the funds was that they be used to support the SARP initiative. D.W.K. is a co-founder and shareholder of OscillaVent, Inc., and is a co-inventor on several patents involving mechanical ventilation. D.W.K. also receives research support from ZOLL Medical Corporation, and has a consultant agreement with Lungpacer Medical, Inc. The authors attests that industry had no role in the preparation, review, or approval of the manuscript.

CRediT authorship contribution statement

Xuan Zhang: Writing – review & editing, Writing – original draft, Visualization, Methodology, Investigation, Formal analysis, Conceptualization. **Prathish K. Rajaraman:** Writing – review & editing, Investigation. **Frank Li:** Writing – review & editing, Investigation. **Sanghun Choi:** Writing – review & editing, Investigation. **Alejandro P. Comellas:** Writing – review & editing. **Eric A. Hoffman:** Writing – review & editing. **Sean B. Fain:** Writing – review & editing. **David W. Kaczka:** Writing – review & editing. **Benjamin M. Smith:** Writing – review & editing. **Jiwoong Choi:** Writing – review & editing. **Mario Castro:** Writing – review & editing. **Sally E. Wenzel:** Writing – review & editing. **Nizar N. Jarjour:** Writing – review & editing. **Mark L. Schiebler:** Writing – review & editing, Conceptualization. **Elliot Israel:** Writing – review & editing. **Bruce D. Levy:** Writing – review & editing. **John V. Fahy:** Writing – review & editing. **Serpil C. Erzurum:** Writing – review & editing. **Andrew Babiskin:** Writing – review & editing. **Minori Kinjo:** Writing – review & editing. **Ross Walenga:** Writing – review & editing. **Ching-Long Lin:** Writing – review & editing, Writing – original draft, Supervision, Investigation, Conceptualization.

[k]Department of Medicine, McGill University Health Centre Research Institute, Montreal, Canada

[l]Division of Pulmonary, Critical Care and Sleep Medicine, University of Kansas School of Medicine, Kansas City, KS, USA

[m]Division of Pulmonary, Allergy, and Critical Care Medicine, University of Pittsburgh, Pittsburgh, PA, USA

[n]School of Medicine & Public Health, University of Wisconsin, Madison, WI, USA

[o]Brigham & Women's Hospital, Harvard Medical School, Boston, MA, USA

[p]Department of Medicine, University of California-San Francisco, San Francisco, CA, USA

[q]Cleveland Clinic, Cleveland, OH, USA

[r]Division of Quantitative Methods and Modeling, Office of Research and Standards, Office of Generic Drugs, Center for Drug Evaluation and Research, U.S. Food and Drug Administration, Silver Spring, MD, USA

[s]Division of Therapeutic Performance II, Office of Research and Standards, Office of Generic Drugs, Center for Drug Evaluation and Research, U.S. Food and Drug Administration, Silver Spring, MD, USA

Abstract

Purpose: This study investigated asthma phenotypes and their associations with ventilation heterogeneity and particle deposition by utilizing Single-Photon Emission Computed Tomography (SPECT) imaging, quantitative Computed Tomography (qCT) imaging-based subgrouping, and a whole-lung computational model.

Materials and methods: Two datasets were analyzed: one from a combined SPECT and CT (SPECT/CT) study with six asthmatic subjects, and another from the Severe Asthma Research Program (SARP) with 209 asthmatic subjects. Data from 35 previously acquired healthy subjects served as a control group. Each subject underwent CT scans at full inspiration and expiration, along with pulmonary function testing (PFT). The SPECT/CT study included ventilation SPECT imaging. Key qCT variables such as airway diameter, wall thickness, percentage of air trapping (AirT%), and percentage of small airway disease (fSAD%) were assessed. A subject-specific whole-lung computational fluid and particle dynamics (CFPD) model predicted airway resistance, particle deposition fraction, and the coefficient of variation (CV) for ventilation heterogeneity. Subjects were categorized into four predefined asthma imaging subgroups/clusters with increasing severity (C1-C4). CFPD-predicted CVs were validated against SPECT measurements. We compared PFT, qCT, and CFPD variables across SARP clusters and analyzed particle deposition fractions in large conducting, small conducting, and respiratory airways.

Results: Cluster C4 exhibited a significantly distinct ventilation profile compared to other clusters and health controls. This distinction contrasted with the insignificant differences between ventilation profiles in severity subgroups defined by conventional spirometry-based guidelines. Airway resistance varied significantly across the asthma clusters. Although both C3 and C4 clusters represented severe asthma, only C4 showed a significant increase in AirT%, primarily due to fSAD%. Since inflammatory phenotypes differ — C3 with wall thickening in large and

small conducting airways, and C4 with elevated fSAD% and Emph% in small conducting and respiratory airways — fine particles (~5 μm) and extrafine particles (~1 μm) are more effective at reaching the respective regions in C3 and C4. Given that C2 and C4 have hyper-responsive phenotypes with narrowed conducting airways, fine particles are more effective in reaching these areas. Airway enlargement in targeted segments of the left lower lobe resulted in improved particle deposition.

Conclusion: Our cluster-informed CFPD-based approach enhances the understanding of ventilation heterogeneity in asthma and holds potential for refining strategies for inhalational therapies.

Keywords

Asthma; CT; SPECT; Clusters; CFPD; Ventilation heterogeneity; Particle deposition

1. Introduction

Asthma is one of the most common lung diseases and manifests as dyspnea, wheezing, and cough (Porsbjerg et al., 2023). Additionally, asthma patients commonly exhibit small airway disease, which poses a challenge in disease management, as these airways are less than 2 mm in diameter (Usmani et al., 2016; Zinellu et al., 2019).

The pathophysiology of asthma is complex and multifaceted. Recent advancements in quantitative Computed Tomography (qCT) imaging have provided new insights into the diverse features of lung diseases (Hoffman, 2022; Choi et al., 2015). Using machine learning, participants with asthma were categorized into distinct clusters based on qCT structural and functional variables (Choi et al., 2017). Cluster 1 (C1) included young, early-onset patients with nonsevere asthma and normal airway structures. In this group, lung function was reversible, and symptoms were easy to manage. Cluster 2 (C2) encompassed patients with both non-severe and severe asthma, characterized by airway narrowing. C2 experienced persistently altered lung function and more difficult to control symptoms. In contrast, clusters 3 (C3) and 4 (C4) consisted predominantly of patients with severe asthma but differed in their characteristics. C3 was marked by airway dilation and wall thickening, while C4 was characterized by airway narrowing and significant air-trapping. Clinically, C3 comprised primarily obese, female-dominant patients with reversible lung function, while C4 predominantly included older, male patients with persistently altered lung functions.

The use of *in vitro* and *in silico* approaches has significantly advanced our understanding of ventilation and particle deposition in the human lung. For example, Schum and Yeh (1980), Yeh and Schum (1980) conducted an *in vitro* study to measure particle deposition in lung regions using a silica-cast airway model, which led to the development of a one-dimensional (1D) deposition model. Concurrently, *in silico* studies introduced subject-specific three-dimensional (3D) computational fluid and particle dynamics (CFPD) models to investigate particle transport and deposition in individuals with asthma (Rajaraman et al., 2020; Zou et al., 2021). Additionally, Kuprat et al. (2023) employed a 3D CFPD model combined with a semi-empirical regional deposition model to simulate deposition in large airways and estimate overall deposition across the respiratory tract. Paul et al. (2021) applied

a 3D CFPD model to estimate particle deposition in the human airway tract. Srivastav et al. (2011) employed a 3D CFPD model focused on deposition in airways from the third to sixth generations, emphasizing the particle trapping process from lobar to segmental airways. Singh et al. (2020) compared particle deposition in healthy human airways to that in airways affected by a glomus tumor. The validity of these computational models has been supported by correlations with *in vivo* studies using Single-Photon Emission Computed Tomography (SPECT) (Zhang et al., 2022; Sadafi et al., 2024). Recently, a cluster-informed CFPD-based approach was employed to examine differences in flow and particle characteristics across post-COVID-19 clusters (Lin et al., 2021; Zhang et al., 2024).

The purpose of this study was to investigate ventilation heterogeneity and particle deposition in subjects with asthma using combined SPECT/CT imaging and CFPD approaches. We hypothesized that the quantitative attributes of imaging clusters could reveal factors contributing to ventilation heterogeneity in asthma, as well as the uneven distribution and penetration of inhaled particles of various sizes. To test this hypothesis, we conducted a combined SPECT/CT study on six participants with asthma for validation of a CT-based, subject-specific whole-lung CFPD model (Zhang et al., 2022) and leveraged an existing large dataset for a more comprehensive analysis. Additionally, we applied a previously defined classification scheme based on qCT variables to categorize participants with asthma into four imaging clusters (Choi et al., 2017). We used CFPD to predict airway resistance and particle deposition. These predictions served as mechanistic physiomic phenotypes linked to inhaled medications and environmental risk factors (Tawhai et al., 2009; Tawhai et al., 2019). We assessed ventilation heterogeneity within each cluster and examined the deposition of fine and extrafine particles in different regions of the respiratory tract during tidal breathing as well as during slow, deep inhalation with a pause. We also investigated the effectiveness of targeted airway enlargement for improving particle deposition efficiency. Finally, we explored correlations between these pulmonary function testing (PFT), qCT, and CFPD variables.

2. Methods

2.1. Image data

Two datasets of patients with asthma were analyzed. The first dataset was collected from a U.S. Food and Drug Administration (FDA)-funded SPECT/CT study on asthmatic small airways, which enrolled a total of six male subjects with asthma at the University of Iowa (UI). The second dataset was acquired from an National Institutes of Health (NIH)-sponsored multicenter study of the Severe Asthma Research Program (SARP) (Wenzel and Busse, 2007). This dataset consists of 209 subjects with asthma previously utilized for clustering analysis (Choi et al., 2017). Additionally, 35 healthy subjects with no prior history of pulmonary disease, previously recruited under a separate IRB approval at UI, were used as a control group (Li et al., 2012). The SPECT/CT data were mainly used for CFPD validation, while the SARP data were used for a more comprehensive statistical inter-cluster analysis against healthy data. Hereafter, the subjects in the first and second datasets are referred to as the “SPECT” subjects and the “SARP” subjects (or clusters), respectively.

For each subject in both datasets, PFT was performed to assess lung function, and a pair of CT scans at full inspiration and expiration was acquired after inhalation of a bronchodilator, following the ATS standard spirometry testing protocol. Specifically, the subjects were initially given 2 puffs with 90 mcg/puff. If the change in FEV_1 was less than 200 mL from baseline, an additional 2 puffs were administered, followed by a 15-minute wait before repeating spirometry. As a result, all SPECT subjects were given 2 puffs except SPECT-4 with 4 puffs. In the SPECT ventilation scan for the SPECT/CT study, technetium-99m (^{99m}Tc) sulfur colloid was used as the radiotracer. It was delivered by a nebulizer, called the IV-600P Insta/vent Plus, with a reported median mass aerodynamic diameter (MMAD) of 0.28 μm. Due to the small cohort in the SPECT/CT study, we enrolled three subjects with non-severe and three with severe asthma based on pre-bronchodilator forced expiratory volume in the first second as percentage of the predicted value (FEV_1%). The study protocol received approval from the IRB at the UI and the Research Involving Human Subjects Committee (RIHSC) at the FDA. Additionally, the Medical Radiation Protection Committee (MRPC) committee at UI has determined that additional Radioactive Drug Research Committee (RDRC) approval was not necessary.

2.2. Image processing and qCT variables

VIDAVision software (VIDA Diagnostics Inc., Coralville, Iowa, USA) was used to segment lung lobes, airways, and vessels from CT images and extract variables such as airway segment length, diameter, and wall thickness. Average hydraulic diameter and wall thickness of segmental airways across the five lobes (sLUL, sLLL, sRUL, sRML, sRLL, where LUL=left upper lobe, LLL=left lower lobe, RUL=right upper lobe, RML=right middle lobe, RLL=right lower lobe, and “s” denotes the segmental branching level) at TLC were calculated. To reduce the effect of individual variability, normalization formulae were used to compute the normalized hydraulic diameter (D_h^*) and normalized wall thickness (W_T^*) using predicted values from healthy subjects based on sex, age, and height (Choi et al., 2015). This approach allowed for the dissociation of wall thickening, a phenotype related to inflammation, from luminal narrowing, a phenotype related to hyper-responsiveness (Choi et al., 2015). Additionally, the homothety ratio (D/D_{parent}), measuring the proportional relationship between the diameters of a branch and its parent branch, was calculated. A decrease in this ratio indicates pulmonary disease, suggesting higher energy dissipation during breathing due to air flow obstruction (Bokov et al., 2014). The Adaptive Multiple Feature Method (AMFM) (Uppaluri et al., 1999) was applied to calculate bronchovascular patterns in all subjects based on TLC scans.

Image registration was utilized to derive functional variables, including the determinant of the corresponding Jacobian matrix (hereafter, called Jacobian, which is a measure of volume expansion from expiratory to inspiratory CT scans, ≥ 1), percentage of air-trapped voxels (AirT%), percentage of functional small airway disease voxels (fSAD%), and percentage of emphysematous voxels (Emph%) across the five lobes and for the whole lung (Choi et al., 2013; Haghighi et al., 2018). Additionally, a fraction threshold-based approach for quantifying AirT%, fSAD%, and Emph% was used to account for protocol differences due to varying CT scanners and breath-hold coaches (Choi et al., 1985).

A total of 57 multiscale qCT variables (32 local, 20 lobar, and 5 global) (Schum and Yeh, 1980; Yeh and Schum, 1980) were derived. The local qCT variables consist of branching angle (θ, the angle between two bifurcated branches), branch circularity (Cr,the ratio of the perimeter of an area equivalent circle to the perimeter of lumen area), W_T^*, and D_h^* in segmental airways. The lobar variables include air ventilation fraction (Vent), AirT%, Jacobian, and anisotropic deformation index (ADI) - a measure of preferential deformation of a local volume (Amelon et al., 2011; Jahani et al., 2017) - in five lobes. The global variables comprise lung shape, ventilation of upper lobes over middle and lower lobes $(U/(M+L)|v)$, as well as Jacobian (Total), AirT% (Total), and ADI (Total) for the whole lung. In this study, we focused on the ten major qCT variables identified previously (Choi et al., 2017), which include Jacobian, AirT%, $D_{h,\ sLLL}^*$, $W_{T,\ sRUL}^*$, $D_{h,\ BronInt}^*$, $Vent_{RUL}$, $Jacobian_{LUL}$, $D_{h,RMB}^*$, $W_{T,\ sRML}^*$, and ADI_{LUL}. Additionally, fSAD%, Emph%, $W_{T,\ BronInt}^*$, and D/D_{parent} were presented. Functional variables such as Jacobian, AirT%, fSAD%, Emph%, Vent, and ADI were derived from image registration, while structural variables D_h^*, W_T^*, and D/D_{parent} were obtained from image segmentation. The subscript indicated the lung region, while variables without a subscript represented measurements for the total lung (with 'Total' omitted). The regions for the functional variables could include the total lung and lobes such as 'RUL' and 'LUL', while the regions for the structural variables could refer to segmental airways in the total lung and within a lobe such as 'sLLL', 'sRUL', and 'sRML', and specific branches like 'RMB' (right main bronchus) and 'BronInt' (right intermediate bronchus). Full names of each variable or region are described in Table S1 in the supplementary material.

2.3. Subject classification

In our previous work, we identified four distinct asthmatic clusters using the aforementioned qCT variables and developed a qCT-based simple classification (SC) scheme that predicts cluster membership with 87% accuracy, using just four key qCT variables (Choi et al., 2017). The four qCT variables for the SC scheme include two global measures: Jacobian (Total) and AirT% (Total), and two local measures: $D_{h,\ sLLL}^*$ in the sLLL and $W_{T,\ BronInt}^*$ for the BronInt (see Fig. S1 in the supplementary material). For comparison, we also classified the subjects according to the guidelines of the National Asthma Education and Prevention Program (NAEPP) (National Asthma Education and Prevention Program TEPotDaMoA 2007) into mild, moderate, and severe asthma, and the American Thoracic Society (ATS) (Chung et al., 2014) into severe and nonsevere asthma.

2.4. CFPD

Airway resistance and particle deposition fraction ($DF\% = \frac{\text{Number of deposited particles}}{\text{Number of inhaled particles}}$) during tidal breathing were simulated using a 1D CFPD model (Zhang et al., 2022). Tidal volume for each subject was determined based on ideal body weight, involving about 520 mL of air. To mimic tidal breathing, a 5-second (s) sinusoidal breathing waveform (2.5 s duration for inhalation and exhalation each) was imposed at the trachea. Particle deposition in the mouth region was estimated using the International Commission on Radiological Protection (ICRP) Human Respiratory Tract Model (HRTM) (Smith, 1994).

To assess ventilation heterogeneity, we calculated the coefficient of variation (CV) of particle distribution. This model was previously validated against SPECT/CT data for COPD subjects (Zhang et al., 2022). In this work, we further validated the model against SPECT/CT data for asthmatic subjects. For SARP subjects, we also simulated activation by a metered dose inhaler with a slow, deep inhalation (1.25 s for fast inhalation and 3.75 s for slow inhalation) followed by a breath hold (pause) (Zhang et al., 2022; Longest et al., 2012), involving an air volume equivalent to the inspiratory capacity (IC) (Choi et al., 2019).

2.5. Statistical analysis

Welch's ANOVA test was used to assess differences between clusters, setting the significance threshold at $p < 0.05$. When Welch's ANOVA test indicated statistically significant differences, Tukey's Honestly Significant Difference (HSD) test was applied for detailed pairwise comparisons, maintaining the same significance level.

To explore the relationships between PFT, qCT, and CFPD variables, we used Pearson's correlation coefficient (r). For clinical analysis (Miot, 2018), correlation strengths were categorized as follows: $|r| \leq 0.3$ as negligible, $0.3 < |r| \leq 0.5$ as weak, $0.5 < |r| \leq 0.7$ as moderate, $0.7 < |r| \leq 0.9$ as strong, and $|r| > 0.9$ as very strong. A p-value of < 0.05 was considered statistically significant. Spearman's correlation coefficient was used for categorical variables, including cluster membership and severity definition based on the NAEPP and ATS guidelines. Categorical variables were one-hot encoded, with 0 indicating that the variable did not belong to the category and 1 indicating that it did. The same categories for correlation strength and significance levels were applied.

When comparing CFPD and SPECT data, we calculated the normalized root-mean-square error (NRMSE; see the supplementary material for details). An NRMSE value below 0.05 indicated good agreement between them, providing confidence in the reliability of our model in predicting actual lung ventilation.

3. Results

This section is organized as follows: First, we present the demographics, PFTs, and classifications of SPECT and SARP subjects, compared to healthy controls. Next, CFPD-predicted CV values for ventilation heterogeneity were validated against those calculated from SPECT data, with differences quantified for both whole lungs and lobes. After validation, we applied CFPD to SARP subjects to investigate cluster-specific ventilation characteristics. To explain these features, we examined distinct qCT structural and functional variables for each cluster. We then applied CFPD to predict airway resistance and particle deposition. Finally, we established correlations among clinical, qCT, and CFPD variables.

3.1. Demographics, PFT, and classification of SPECT and SARP subjects

Table 1 presents the demographic and PFT data for the six SPECT subjects. According to the NAEPP (or ATS) guidelines, the first three subjects were classified as having mild (or nonsevere) asthma, while the remaining three were classified as having moderate-to-severe (or severe) asthma. Using the SC scheme (Fig. S1) (Choi et al., 2017), the first three subjects were categorized as C1, while one of the remaining three subjects was categorized as C4.

Additionally, the SARP subjects were classified into four distinct clusters: C1 (n=76), C2 (n=41), C3 (n=55), and C4 (n=37). Table 2 presents the demographic and PFT data for these clusters. According to the demographic information, C1 subjects were the youngest, while C4 subjects were the oldest. C3 had a significantly higher BMI and a greater percentage of females compared to the other clusters. Compared to the healthy control group, FEV_1 % predicted and FEV_1/forced vital capacity (FVC) declined with increasing cluster number. With the NAEPP criteria, C1, C2, and C3 were mostly composed of mild asthma. With the ATS guidelines, C1 had 39.5% nonsevere asthma and C2 had 52.5% nonsevere asthma. C3 and C4 had more than 70% severe asthma (see Fig. S2 for the correlations between subgroups).

3.2. CFPD validation

The results from the 1D CFPD analysis were validated against both the SPECT/CT *in vivo* data and the 3D CFPD *in silico* data (Choi et al., 2019). For each SPECT subject, we compared the CV of tracer ^{99m}Tc concentration with the corresponding CFPD-predicted value. Since the size of ^{99m}Tc sulfur colloid is below 1.0 μm, the particle diameter for the CFPD simulations was set as 0.5 μm. Fig. 1 shows that the SPECT-measured ventilation CV values and the corresponding CFPD-predicted values for all six subjects were in good agreement, with NRMSE < 0.05. Moreover, the NRMSE between SPECT and CFPD lobar CV values is less than 0.05.

To compare the 3D CFPD results in CT-resolved airways with a slow and deep inhalation (Choi et al., 2019), 1D CFPD simulations with the same waveform were performed for the SARP subjects. The lobar deposition fractions predicted by the 3D CFPD were compared with those of the 1D CFPD. Fig. 2(a) and (b) compare the lobar deposition fractions in C1 and C4 subjects for 1.0 μm and 8.0 μm particles, respectively. The results showed good agreement between 1D and 3D CFPD data, with NRMSE < 0.05.

3.3. Ventilation heterogeneity

Fig. 3 displays the CV values of the SARP clusters, along with those of healthy subjects, showing means (SD) of 0.46 (0.04) for healthy subjects and 0.47 (0.04), 0.49 (0.05), 0.42 (0.02), and 0.55 (0.04) for C1, C2, C3, and C4, respectively. Notably, C4 exhibited the highest CV compared to others ($p < 0.001$), indicating a more heterogeneous ventilation within their lungs. C2 also had elevated CV, but it only significantly differed from C3 ($p < 0.01$), which had the lowest CV among all clusters (see Fig. S3 for the spatial distribution of inhaled 0.5-μm particles and the corresponding CV in each cluster archetype). Fig. 4(a) compares the CV values of the SARP subgroups defined by the NAEPP criteria, while Fig. 4 (b) shows those defined by the ATS guidelines. In contrast to qCT-based classification, the variations in ventilation heterogeneity among the NAEPP- and ATS-defined subgroups were not statistically significant.

3.4. qCT variables

Table 3 shows the key qCT variables for each SARP cluster. The C2, C3, and C4 clusters exhibited a significant reduction in Jacobian and ADI values, with the most pronounced reduction in the C4 cluster. Additionally, C4 showed a notable increase in AirT% and

fSAD%. Regarding airway narrowing, C2 and C4 had reduced normalized hydraulic airway diameters in the BronInt, RMB, and segmental branches of the LLL. Airway wall thickening was observed in C3, particularly in the segmental branches of the RUL and RML, as well as in the BronInt. It is worth noting that over 90% of CT-resolved airway segments used in calculating $D^*_{h,sLLL}$ and $W^*_{T,sRUL}$ are large conducting airways (D > 2 mm). The four qCT phenotypes used in the SC scheme (Fig. S1) included reduction in lung deformation (Jacobian↓), increase in air trapping/small airway disease (AirT%/fSAD%↑), airway narrowing (D^*_h ↓), and wall thickening (W^*_T ↑), where ↓ and ↑ denote decrease and increase, respectively. In general, among all clusters, C1 exhibited the highest Jacobian value, indicating mild reduction in lung deformation, while C4 had the lowest Jacobian value, reflecting significant reduction in lung deformation. The C2 and C4 clusters exhibited airway narrowing, while C3 was characterized by both airway dilation and wall thickening. Additionally, only C4 was characterized by significant small airway disease. The statistical inter-cluster comparisons of the functional variables (AirT%, fSAD%, Emph%, and Jacobian) and structural variables (D^*_h and WT*) are presented graphically in Figs. S4 and S5, respectively. The average homothety ratio observed in healthy controls was within the previously reported range of 0.80 to 0.85 for healthy subjects (Wenzel and Busse, 2007). Additionally, in C4 and SPECT-6, the homothety ratio was notably below the theoretical critical minimum value of 0.79, as shown in Tables 3 and 4 as well as Fig. S6, indicating airway remodeling.

To better understand the qCT-based classification scheme, Table 4 lists the key qCT variables for the SPECT subjects. Three of the six subjects (SPECT-1, SPECT-2, and SPECT-6) had matching qCT-based and spirometry-based classifications. The three nonsevere subjects (SPECT-1, SPECT-2, and SPECT-3) had Jacobian values greater than the threshold of 2.21 (Fig. S1), classifying them in the C1 cluster. The only severe subject (SPECT-6) that was classified as C4 exhibited a significant reduction in lung deformation (Jacobian↓) and an increase in AirT%, due to a rise in fSAD%. SPECT-4, also a severe subject, was classified as C1 due to a Jacobian value greater than 2.21 and insignificant AirT%, despite a significant decline in FEV_1% predicted. The relatively higher Jacobian value may be attributed to receiving 4 puffs of bronchodilator instead of 2 puffs. SPECT-5 was classified in the C2 cluster due to a moderate reduction in Jacobian and airway narrowing as well as insignificant AirT%, despite a significant decline in FEV_1% predicted. Based on (Choi et al., 2017), C2 subjects included both nonsevere and severe asthma, indicating that PFT alone is insufficient to differentiate asthmatic subgroups.

To further understand how these qCT structural and functional characteristics affect ventilation heterogeneity, Fig. 3 plots the CV values of the SPECT subjects for comparison with those of the SARP clusters. The three subjects with matching classifications (SPECT-1, SPECT-2, and SPECT-6) exhibited consistent CV with their respective clusters. SPECT-3 (C1, nonsevere asthma) demonstrated more heterogeneous ventilation (CV ↑) due to airway narrowing. Although SPECT-4 and SPECT-5 had severe asthma defined by spirometry, their corresponding lung deformations were mild to moderate, with essentially no small airway disease, resulting in more homogeneous ventilation (CV↓) than C4 subjects.

To investigate whether subjects exhibiting mismatching classifications, like SPECT-3, SPECT-4, and SPECT-5, also existed among the SARP subjects, we identified SARP-3 and SARP-4 among the C1 subjects and SARP-5 among the C2 subjects, as shown in Table 4. In other words, SARP-3, SARP-4, and SARP-5 corresponded to SPECT-3, SPECT-4, and SPECT-5, respectively, in terms of major qCT imaging metrics and ventilation heterogeneity profiles. The results thus suggest the presence of sub-clusters within these four imaging clusters.

3.5. CFPD-based airway resistance and particle deposition

Fig. 5 shows the airway resistance by lobe for the SARP clusters. The results indicate that the C2 and C4 clusters exhibited increased airway resistance compared to healthy controls, which aligns with airway narrowing observed in these clusters. Among all the asthmatic clusters, C3 showed the lowest airway resistance.

Fig. 6(a) presents the whole lung deposition fractions for particles ranging from 0.01 to 10.0 μm across all clusters and healthy controls. Particles sized 0.4–0.5 μm had the lowest deposition fraction across all groups. Notably, C4 had the lowest deposition fraction of any group, regardless of particle size ($p<0.05$). This finding suggests that the structural and functional changes in C4 subjects significantly impact their ability to effectively deposit particles in the lungs.

To account for the particle deposition in the mouth-throat (MT) region ($DF\%_{MT}$) during mouth breathing, the $DF\%_{MT}$ estimated from the ICRP HRTM model (Smith, 1994) was displayed in Fig. 6(b), the DF% values for SARP clusters were recalculated based on (1-$DF\%_{MT}$) × DF% predicted from the 1D CFPD in Fig. 6(a). $DF\%_{MT}$ is negligible for 0.1–1.0 μm particles, and increases quickly to about 70% at 10 μm. The resulting DF% in the whole lungs peaks at about 4 μm in Fig. 6(b).

To investigate the penetration of inhaled particles, the total deposition fraction was further divided into three regions based on the average airway diameter (D): large airways ($D \geq 2$ mm), small airways ($D < 2$ mm), and respiratory airways. Fig. 7 shows the particle deposition fractions by region for particle sizes of 0.01 μm, 0.1 μm, 1.0 μm, 5.0 μm, and 10.0 μm. Fig. 7(a,b,c) on the left panel was based on tidal breahing, while Fig. 7(d,e,f) on the right panel was based on slow, deep breating with a 10-s pause. Overall, the results indicate that 1.0 and 0.1 μm extrafine particles penetrate deeper into the lungs, reaching the respiratory region. In contrast, 5.0 μm fine particles are distributed more uniformly across the three regions. Notably, 0.01 μm nanoparticles exhibited the highest deposition in the small airways. Meanwhile, 10 μm large particles were predominantly trapped in the mouth-throat area, with the highest deposition occurring in the large airways. With slow, deep inhalation and a pause, more particles are deposited deeper into the lungs, with the most notable increase observed for 1.0 μm particles in the respiratory region. Additionally, significant inter-cluster variations were evident, as highlighted in the figure.

3.6. Correlations between variables and associations with clusters

Fig. 8 shows the heat map of the correlation coefficients between PFT, qCT, and CFPD variables. All correlations are positive unless otherwise noted as negative. The results are summarized by three categories of variables: PFT, qCT, and CFPD.

In the PFT category, FEV1 % predicted and FEV1/FVC are moderately correlated. Both measures demonstrate a moderate negative correlation with high attenuation patterns in images, such as AirT%, Emph %, and fSAD%. Additionally, FEV_1 % predicted and FEV_1/FVC exhibit a weak correlation with Jacobian. FEV_1 % predicted also shows a weak correlation with D_h^* and a weak negative correlation with resistance.

For the qCT variables, fSAD% and AirT% are correlated with Jacobian (moderate negative), D/D_{parent} (weak negative), resistance (weak), DF% (both weak and moderate negative), and CV (moderate). Jacobian correlates with fSAD% and AirT% (moderate negative) and DF% (strong). D_h^* has a weak negative correlation with resistance and CV, while D/D_{parent} shows a weak negative correlation with resistance.

In the CFPD category, Resistance, DF%, and CV are examined. Resistance is correlated with FEV_1 % predicted (weak negative) and CV (moderate). It is also correlated with qCT variables, including fSAD% and AirT% (weak), D_h^* (weak negative), and D/D_{parent} (weak negative). Furthermore, resistance exhibits a negligible correlation with Jacobian. DF% shows a strong correlation with Jacobian and a weak to moderate negative correlation with fSAD/AirT%, while it has no correlation with CV. Lastly, CV is correlated with resistance (moderate), fSAD%, and AirT % (moderate), and D_h^* (weak negative).

Fig. 9 shows the heat map of Spearman's correlation coefficients between clusters and variables. The results reveal that C1 primarily consisted of younger individuals. C2 had a weak association with a reduction in Jacobian. C3 had a weak but significant correlation with BMI, airway diameter, and wall thickness, as well as a weak negative correlation with resistance. In contrast, C4 exhibited a moderate negative correlation with both FEV_1 % predicted and FEV_1/FVC. Additionally, C4 was strongly correlated with fSAD% and AirT%, and moderately correlated with Emph%. There was also a moderate correlation with both resistance and CV among C4 subjects.

Regarding the cluster correlations with the four qCT variables used in the SC scheme, C1 had a strong correlation with Jacobian. In contrast, C2 and C4 exhibited weak negative correlations with Jacobian, while C3 displayed a marginal weak negative correlation. C4 had a strong correlation with fSAD% and AirT%, and C3 was moderately correlated with airway diameter and weakly but significantly correlated with wall thickness. C2 and C4 had marginal negative correlations with airway diameter. Overall, Jacobian effectively distinguished C1 from C2, C3, and C4. AirT% further differentiated C4 from C2 and C3. C3 was set apart from C2 by airway dilation and wall thickening, while C2 was primarily characterized by airway narrowing and Jacobian reduction.

3.7. Airway enlargement and breath hold

Airway narrowing in the LLL ($D^*_{h,sLLL}$) is a key phenotype in C4 severe asthmatic subjects (Table 3). The diameter of the left lower bronchus (LLB), also known as the trifurcation of the LLB (TriLLB), significantly contributed to the loadings of D^*_h in the principal component analysis (Choi et al., 2017). 3D CFPD analysis further revealed that the constricted LLB in a C4 subject created a local hotspot with high particle deposition density at the first bifurcation downstream of the LLB during inspiration (Choi et al., 2019). Based on these previous findings, two key questions needed to be addressed. First, is the local hotspot observed in the 3D CFPD analysis of a C4 subject (Choi et al., 2019) also present in the C4 cluster? Second, how do LLB enlargement and a breath hold affect particle deposition in the LLL? The second question is partly motivated by bronchial thermoplasty, a medical procedure used to treat severe asthma (Castro et al., 2010; Castro and Chupp, 2020), and aims to quantify its effectiveness in terms of improving particle deposition. A pause is known to increase deposition in deep lung regions (Zhang et al., 2022; Hofemeier et al., 2018; Koullapis et al., 2018; Koullapis et al., 2020). Thus, in the following analysis, a 1-s pause was incorporated at the end of slow and deep inhalation.

The left side of Fig. 10(a) shows a 3D airway model (Choi et al., 2019), featuring CT-resolved airways and five paths extending from terminal CT-resolved branches to terminal bronchioles, one in each of the five lobes. The branches highlighted in yellow, along with the corresponding red-coded 1D skeleton, illustrate a typical network branching from the LLB in the LLL (Choi et al., 2019). In the analysis, particle deposition in this typical network was compared with that in the entire LLL for particle sizes of 1, 2, 4, and 8 μm. Fig. 10(a) shows that the deposition fractions in the typical network for SARP subjects predicted by 1D CFPD closely match those calculated previously using 3D CFPD (Choi et al., 2019). As particle size increased, deposition fractions in C4 were significantly higher compared to other clusters, a trend also observed in C2 due to airway narrowing in the LLL. Larger particles tended to deposit in larger branches, while airway narrowing further increased regional deposition heterogeneity. However, this increased local deposition did not translate to higher deposition across the entire LLL (Fig. 10(b)). The narrowed LLB in C4 created a local region with high particle concentration, trapping over 50% of large particles entering the LLL. Additionally, the reduced inspiratory capacity in C4 may have resulted in fewer particles reaching the deep lung regions.

Fig. 11 shows the lobar deposition efficiency in the lobar branch LLB $\left(DE\%_{LLB} = \frac{\text{Number of particles deposited in LLB}}{\text{Number of particles enteing LLL}}\right)$ and entire LLL $(DE\%_{LLL} = \frac{\text{Number of particles deposited in LLL}}{\text{Number of particles enteing LLL}})$ of a C4 subject (SPECT-6) under three conditions with slow and deep inhalation: (Porsbjerg et al., 2023) a 20% dilation of the LLB diameter (no pause), (Usmani et al., 2016) with a 1-s pause (no LLB dilation), and (Zinellu et al., 2019) a 20% LLB dilation and a 1-s pause. For 1.0 μm particles, dilation of the LLB resulted in a 2.4% increase in $DE\%_{LLL}$, while the pause led to a 6.2% increase. With both dilated LLB and pause, the enhancement of $DE\%_{LLL}$ rose to 9.8%. $DE\%_{LLB}$ accounted for only 14% of the $DE\%_{LLL}$. For 8.0 μm particles, LLB dilation resulted in a 3.9% increase in $DE\%_{LLL}$ but reduced $DE\%_{LLB}$ by 0.6%. With a pause, $DE\%_{LLB}$ and $DE\%_{LLL}$ increased by

2.9% and 10.4%, respectively. When both dilation and pause applied, $DE\%_{LLL}$ increased by 16.5%. While branch dilation allowed more particles to enter and deposit in the downstream of LLB, a pause enhanced deposition by providing more time for particles to settle in airway segments, thereby improving the deposition across all segments.

4. Discussion

Recent advancements in imaging technologies allowed for quantitative and sensitive measurements of local structural and functional changes in individuals with asthma (Hoffman, 2022). Our study aimed to correlate predefined imaging clusters with ventilation heterogeneity in patients with asthma and explore the implications for inhaled drug delivery. By combining qCT-based classification with subject-specific whole-lung CFPD, our goal was to enhance patient stratification and propose strategies to optimize the deposition of inhaled therapeutic aerosols in targeted lung regions of the patients with asthma.

The qCT-based classification scheme utilizes two global variables—Jacobian (Total) and AirT% (Total)—and two local variables—$D^*_{h,\,sLLL}$ and $W^*_{T,\,BronInt}$ (see Fig. S1). A high threshold for Jacobian (Total) distinguishes C1 from the other clusters. A high threshold for AirT% (Total) combined with a low threshold for Jacobian (Total) further differentiates C4 from C2 and C3. C2 and C3, with intermediate reduction in Jacobian (Total), were distinguished by meeting the criteria of a low $D^*_{h,\,sLLL}$ and a high $W^*_{T,\,BronInt}$, respectively. Consequently, C1 was characterized by mild reduction in lung deformation, C2 by airway narrowing, C3 by wall thickening, and C4 by significant reduction in lung deformation and air trapping. In general, this scheme reflects the severity stage in asthmatic subjects when compared with NAEPP- and ATS-defined subgroups (Table 2 and Fig. S2). Fig. 3 underscores the effectiveness of this scheme in distinguishing C4, which exhibits a significantly distinct ventilation profile compared to other clusters. This distinction contrasts with the insignificant differences between ventilation profiles in severity subgroups defined with NAEPP and ATS guidelines (see Fig. 4).

Both FEV_1 % predicted and FEV_1/FVC, which measure airflow obstruction, were reported to be positively correlated with Jacobian (Cohen et al., 2022). This indicates that reduced lung deformation is associated with asthma. Our analysis supports this finding, though the correlation is weak but significant ($p < 0.05$). Specifically, C3 showed a moderate decrease in Jacobian, while C2 and C4 experienced a more significant reduction (Choi et al., 2015; Choi et al., 2017). Airflow obstruction in asthmatics was also linked to an increase in AirT% (Choi et al., 2015; Choi et al., 2017; Park et al., 2012). Our findings consistently showed that FEV_1% predicted and FEV_1/FVC exhibited a moderate negative correlation with AirT%. In the C1 cluster, which consisted predominantly of mild asthmatics, AirT% was comparable to healthy controls. However, in severe asthma, there were notable differences: AirT% is 7.22% ± 0.62% in C3 and significantly increases to 24.92% ± 10.13% in C4 (Table 3). This substantial rise in AirT% in C4 was largely attributed to an increase in small airway disease, as quantified by fSAD %. In C4, fSAD% and Emph% were 15.28% ± 0.76% and 6.47% ± 0.62%, respectively. In addition to changes in lung function, an increased bronchovascular percentage (%) was observed in C2, C3, and C4 compared to healthy subjects (Table 3). While asthma subjects in SARP had significantly higher bronchovascular

percentage (%) compared to heatlhy (SARP: 12.19% ± 2.21% vs healthy: 11.79% ± 1.34%), the differences of bronchovascular percentage (%) among asthma clusters are insignificant. The heightened vasculature indicates inflammation, marked by a continuous influx of mast cells, neutrophils, eosinophils, and inflammatory mediators (Harkness et al., 2015).

We have previously reported that 43% of asthmatic subjects in the C4 cluster showed increased eosinophil counts, and 78% had elevated neutrophil counts based on sputum inflammatory tests (Choi et al., 2017). Together with increased neutrophil counts from BAL tests, the subjects in the C4 cluster likely had neutrophil-dominant asthma. In contrast, C2 exhibited marginal to no inflammation. Both the C2 and C4 clusters were characterized by reduced airway diameters. This regional airway narrowing, along with reduced FEV_1% predicted, is indicative of a phenotype associated with hyper-responsiveness (Bradding et al., 2024). Additionally, C4 was marked by elevated fSAD%, an inflammatory phenotype in the small airways that may contribute to the development of emphysema in the respiratory airways.

In contrast to C2 and C4, C3 was characterized by airway dilation and wall thickening in both large and small airways (Table 3, about 90% of CT-resolved airways in sLLL and sRUL are large airways), presenting inflammation phenotypes distinct from those in C4. Additionally, C3 had a significant decrease in blood lymphocyte counts and an increase in neutrophil counts, resulting in a higher neutrophil-to-lymphocyte ratio (NLR) (Choi et al., 2017). The median of methacholine provocative concentration resulting in 20% decrease in FEV_1 (PC_{20}) in C3 was much lower than in other clusters. Bronchiectasis, also known as pathological bronchial dilation, is a chronic respiratory condition characterized by widened airways, with increased prevalence among patients with severe asthma (Matsumoto, 2022; Ma et al., 2021). While an elevated NLR is a biomarker for bronchiectasis exacerbation (Georgakopoulou et al., 2020), further study is needed to determine whether the inflammation in C3 is related to comorbid bronchiectasis.

Short-acting beta-2-adrenergic agonists (SABAs) and long-acting beta-2-adrenergic agonists (LABAs) are bronchodilators that relax airway smooth muscles, increase airway diameter, and improve air flow. SABAs provide quick relief from acute bronchoconstriction, while LABAs are used for maintenance therapy. Corticosteroids reduce airway inflammation and edema, also associated with asthma. LABAs and inhaled corticosteroids (ICSs) are often used together for long-term control of asthma symptoms, with LABAs relaxing airway muscles and ICSs reducing and preventing swelling. According to (Choi et al., 2017), C3 and C4 consisted of subjects receiving high-dose LABAs and ICSs. Studies have targeted the peripheral airways in asthmatics with extrafine LABAs and ICSs (Postma et al., 2017; Manoharan et al., 2016). Pharmaceutical particle formulations with a MMAD of 2–4 μm are considered fine, while those with an MMAD of 1 μm are classified as extrafine (Postma et al., 2017). In other studies, particles with an MMAD of 2–5 μm are referred to as standard size, and those with an MMAD less than 2 μm are classified as extrafine (El Baou et al., 2017). Particles smaller than 0.1 μm are known as nanoparticles. Sedimentation dominates deposition for particles 5 μm and larger, while Brownian motion and laminar diffusion are more significant for particles 0.1 μm and smaller. For 1 μm particles, all three mechanisms are influential (Zhang et al., 2022).

Hereafter, we focus on the CFPD-based deposition fractions of 1 μm and 5 μm particles, representing extrafine and fine particles, respectively, in large conducting, small conducting, and respiratory airways. These fractions are categorized by cluster and examined under conditions of tidal breathing, as well as slow and deep inhalation with a pause (Fig. 7). Deposition fractions in the mouth-throat region were approximated at 0.25% and 22.5% for 1 μm and 5 μm particles, respectively. Slow and deep inhalation with a pause can double the deposition fraction of extrafine particles in the respiratory region compared to tidal breathing. Additionally, targeting airway enlargement at a single branch in the LLB of C4 subjects could further improve the DF% of both fine and extrafine particles in the LLL by about 10% or more with a longer pause, and reduce the hotspot effect.

In conjunction with qCT-based cluster-specific phenotypes—such as normal airway structure in C1; a hyperresponsive phenotype with narrowing in the large and small airways of C2 and C4; an inflammatory phenotype with wall thickening in C3; and inflammatory phenotypes characterized by elevated fSAD% and Emph% in C4— we propose several strategies to improve the targeted delivery of fine and extrafine particles, which can be tested in future studies. For the delivery of SABAs and LABAs, fine particles around 5 μm should be directed to both the large and small conducting airways in the C2 and C4 clusters, where airway narrowing is prominent. Conversely, in the C1 and C3 clusters, where airway narrowing is less significant, SABAs and LABAs may have limited effects. Given the different inflammation phenotypes, fine particles around 5 μm should be used for ICS delivery to target the conducting airways in C3, while extrafine particles should be used to effectively reach the small conducting and respiratory airways in C4. In the C4 cluster, the delivery of extrafine ICS could be optimized by adopting a slow and deep inhalation technique with a pause. For example, in our CFPD analysis, $DF\%_{Respiratory,\ 1\mu m} = 18.5 \pm 3.9$ with tidal breathing, which increased to $DF\%_{Respiratory,\ 1\mu m} = 35.8 \pm 7.1$ with slow and deep breathing with a pause. For targeting the delivery of fine particles throughout the entire airway tree, tidal breathing may be just as effective as slow, deep inhalation with a pause. Finally, improving deposition fractions for both fine and extrafine particles may be possible by targeting airway enlargement at branch LLB in C4.

Additionally, our CFPD results reveal significant differences in airway resistance among asthmatic clusters (Fig. 5). This finding has important clinical implications that need to be confirmed in future studies. Oscillometry has been used to measure airway resistance and reactance in asthma and COPD (Kaminsky et al., 2022; Kaczka and Dellaca, 2011; Galant et al., 2017). In the current SPECT/CT study, the inclusion criteria were primarily based on FEV_1 % predicted. A future question to explore is whether oscillometry could differentiate resistance among asthmatic clusters, particularly between C1 and C2 and between C3 and C4 (King et al., 2020). Given the limited accessibility of CT, if oscillometry proves effective in detecting these differences, combining spirometry with oscillometric measurements could provide alternative clinical variables for more precise classification of asthmatics than spirometry alone. This approach could be used alongside the previously proposed strategies for delivering inhaled drug aerosols.

5. Limitations

This study has several limitations. First, the sample size for the SPECT/CT study is limited due to high costs, resulting in a relatively small cohort. Additionally, the spirometry-based inclusion criteria cannot differentiate between severe asthma cases with and without air trapping. Second, suggestions regarding the use of fine and extrafine particles for treating different asthmatic cluster subjects still need to be validated through future studies involving human subjects. Third, there may be additional sub-clusters that are not captured by the current predefined imaging clusters. Fourth, the 1D CFPD model is limited to using averaged data along the radial direction of an airway segment and does not account for morphological variations in diseased acini.

6. Conclusions

This study evaluated the effectiveness of qCT-based classification in distinguishing ventilation heterogeneity among asthmatic subjects and explored the implications for delivery of inhaled drug aerosols. We combined imaging and modeling approaches, using new SPECT/CT data for model validation and leveraging existing SARP data for a more comprehensive statistical analysis.

Our findings indicated that imaging clusters, defined by measurable qCT structural and functional changes, distinctly captured varying ventilation characteristics among different asthma clusters. Clusters C2 and C4 exhibited airway narrowing, while C3 and C4 displayed distinct inflammatory phenotypes. C3 was marked by airway dilation and wall thickening, whereas C4 showed a significant increase in air trapping, primarily due to an escalation in small airway disease. Our CFPD analyses suggest that using appropriate aerosol sizes and breathing patterns may improve the delivery of drug aerosols to regions characterized by these unique phenotypes. In summary, this study demonstrates that combining imaging and modeling approaches can provide insights into ventilation heterogeneity and particle deposition in asthma, and generate new hypotheses for future research.

Supplementary Material

Refer to Web version on PubMed Central for supplementary material.

Acknowledgments

This work was supported in part by FDA U01-FD005837, NIH R01-HL168116, NIH R01-HL130506, ED P116S210005, and the Office of the Assistant Secretary of Defense for Health Affairs, Peer Reviewed Medical Research Program, Awards W81XWH-21-1-0507 and W911NF-23-1-0004. Views expressed in this work do not necessarily reflect the official policies of the Department of Health and Human Services and may not be quoted as being made on behalf of a reflecting the position of the U.S. Food and Drug Administration; nor does any mention of trade names, commercial practices, or organization imply endorsement by the United States Government. Opinions, interpretations, conclusions, and recommendations are those of the authors, and are not necessarily endorsed by the Department of Defense.

The authors would like to thank the SARP clinical coordinators and laboratory personnel for their contribution to fulfilling SARP's scientific mission. The research findings resulting from SARP would not have been possible without their dedication and assistance with study visits, data collection, and biological sample processing. The following companies provided financial support for study activities at the Coordinating and Clinical Centers

beyond the third year of patient follow-up: AstraZeneca, Boehringer-Ingelheim, Genentech, GlaxoSmithKline, Sanofi–Genzyme–Regeneron, and TEVA.

Data availability

Data will be made available on request.

References

Amelon R, Cao K, Ding K, Christensen GE, Reinhardt JM, Raghavan ML., 2011. Three-dimensional characterization of regional lung deformation. J. Biomech. 44 (13), 2489–2495. 10.1016/j.jbiomech.2011.06.009. [PubMed: 21802086]

Bokov P, Mauroy B, Mahut B, Delclaux C, Flaud P, 2014. Homothety ratio of airway diameters and site of airway resistance in healthy and COPD subjects. Respir. Physiol. Neurobiol. 191, 38–43. 10.1016/j.resp.2013.10.015. [PubMed: 24200643]

Bradding P, Porsbjerg C, Côté A, Dahlén SE, Hallstrand TS, Brightling CE., 2024. Airway hyperresponsiveness in asthma: The role of the epithelium. J. Allergy Clin. Immunol. 153 (5), 1181–1193. 10.1016/j.jaci.2024.02.011. [PubMed: 38395082]

Castro M, Chupp G, 2020. Updated Asthma Guidelines: Bronchial thermoplasty in the management of asthma. J. Allergy Clin. Immunol. 147 (5), 1638–1639. 10.1016/j.jaci.2021.02.024, 2021.

Castro M, Rubin AS, Laviolette M, Fiterman J, De Andrade Lima M, Shah PL, Fiss E, Olivenstein R, Thomson NC, Niven RM, Pavord ID, Simoff M, Duhamel DR, McEvoy C, Barbers R, NH TH, Wechsler ME, Holmes M, Phillips MJ, Erzurum S, Lunn W, Israel E, Jarjour N, Kraft M, Shargill NS, Quiring J, Berry SM, Cox G, 2010. Effectiveness and safety of bronchial thermoplasty in the treatment of severe asthma: a multicenter, randomized, double-blind, sham-controlled clinical trial. Am. J. Respir. Crit. Care Med. 181 (2), 116–124. 10.1164/rccm.200903-0354OC. [PubMed: 19815809]

Choi S, Hoffman EA, Wenzel SE, Castro M, Lin CL., 1985. Improved CT-based estimate of pulmonary gas trapping accounting for scanner and lung-volume variations in a multicenter asthmatic study. J. Appl. Physiol. 117 (6), 593–603. 10.1152/japplphysiol.00280.2014, 2014

Choi S, Hoffman EA, Wenzel SE, Tawhai MH, Yin Y, Castro M, Lin CL., 2013. Registration-based assessment of regional lung function via volumetric CT images of normal subjects vs. severe asthmatics. J. Appl. Physiol. 115 (5), 730–742. 10.1152/japplphysiol.00113.2013, 1985Epub 20130606 [PubMed: 23743399]

Choi S, Hoffman EA, Wenzel SE, Castro M, Fain SB, Jarjour NN, Schiebler ML, Chen K, Lin C-L, 2015. Quantitative assessment of multiscale structural and functional alterations in asthmatic populations. J. Appl. Physiol. 118 (10), 1286–1298. 10.1152/japplphysiol.01094.2014. Bethesda, Md1985Epub 2015/03/26 [PubMed: 25814641]

Choi S, Hoffman EA, Wenzel SE, Castro M, Fain S, Jarjour N, Schiebler ML, Chen K, Lin CL, 2017. Quantitative computed tomographic imaging–based clustering differentiates asthmatic subgroups with distinctive clinical phenotypes. J. Allergy Clin. Immunol. 140 (3), 690–700. 10.1016/j.jaci.2016.11.053e8. [PubMed: 28143694]

Choi J, LeBlanc LJ, Choi S, Haghighi B, Hoffman EA, O'Shaughnessy P, Wenzel SE, Castro M, Fain S, Jarjour N, Schiebler ML, Denlinger L, Delvadia R, Walenga R, Babiskin A, Lin CL, 2019. Differences in particle deposition between members of imaging-based asthma clusters. J. Aerosol. Med. Pulm. Drug Deliv. 32 (4), 213–223. 10.1089/jamp.2018.1487. [PubMed: 30888242]

Chung KF, Wenzel SE, Brozek JL, Bush A, Castro M, Sterk PJ, Adcock IM, Bateman ED, Bel EH, Bleecker ER, Boulet LP, Brightling C, Chanez P, Dahlen SE, Djukanovic R, Frey U, Gaga M, Gibson P, Hamid Q, Jarjour NN, Mauad T, Sorkness RL, Teague WG., 2014. International ERS/ATS guidelines on definition, evaluation and treatment of severe asthma. Eur. Respir. J. 43 (2), 343–373. 10.1183/09031936.00202013. [PubMed: 24337046]

Cohen J, Shekarnabi M, Destors M, Tamisier R, Bouzon S, Orkisz M, Ferretti GR, Pépin JL, Bayat S, 2022. Computed tomography registration-derived regional ventilation indices compared to global lung function parameters in patients with COPD. Front. Physiol. 13, 862186. 10.3389/fphys.2022.862186. [PubMed: 35721545]

El Baou C, Di Santostefano RL, Alfonso-Cristancho R, Suarez EA, Stempel D, Everard ML, Barnes N, 2017. Effect of inhaled corticosteroid particle size on asthma efficacy and safety outcomes: a systematic literature review and meta-analysis. BMC Pulm. Med. 17 (1), 31. 10.1186/s12890-016-0348-4. [PubMed: 28173781]

Galant SP, Komarow HD, Shin HW, Siddiqui S, Lipworth BJ., 2017. The case for impulse oscillometry in the management of asthma in children and adults. Ann. Allergy Asthma Immunol. 118 (6), 664–671. 10.1016/j.anai.2017.04.009. [PubMed: 28583260]

Georgakopoulou VE, Trakas N, Damaskos C, Garmpis N, Karakou E, Chatzikyriakou R, Lambrou P, Tsiafaki X, 2020. Neutrophils to lymphocyte ratio as a biomarker in bronchiectasis exacerbation: a retrospective study. Cureus 12 (8), e9728. 10.7759/cureus.9728. Epub 20200813 [PubMed: 32944447]

Haghighi B Jr., Choi S, Choi J, Hoffman EA, Comellas AP, Newell JD, Graham Barr R, Bleecker E, Cooper CB, Couper D, Han ML, Hansel NN, Kanner RE, Kazerooni EA, Kleerup EAC, Martinez FJ, O'Neal W, Rennard SI, Woodruff PG, Lin CL, 2018. Imaging-based clusters in current smokers of the COPD cohort associate with clinical characteristics: the SubPopulations and Intermediate Outcome Measures in COPD Study (SPIROMICS) Respir. Res. 19 (1), 178. 10.1186/s12931-018-0888-7.

Harkness LM, Ashton AW, Burgess JK., 2015. Asthma is not only an airway disease, but also a vascular disease. Pharmacol. Ther. 148, 17–33. 10.1016/j.pharmthera.2014.11.010. [PubMed: 25460035]

Hofemeier P, Koshiyama K, Wada S, Sznitman J, 2018. One (sub-)acinus for all: Fate of inhaled aerosols in heterogeneous pulmonary acinar structures. Eur. J. Pharm. Sci. 113, 53–63. 10.1016/j.ejps.2017.09.033. [PubMed: 28954217]

Hoffman EA., 2022. Origins of and lessons from quantitative functional X-ray computed tomography of the lung. Br. J. Radiol. 95, 20211364. 10.1259/bjr.20211364, 1132Epub 20220301 [PubMed: 35193364]

Jahani N, Choi S, Choi J, Haghighi B, Hoffman EA, Comellas AP, Kline JN, Lin C-L, 2017. A four-dimensional computed tomography comparison of healthy and asthmatic human lungs. J. Biomech. 56, 102–110. 10.1016/j.jbiomech.2017.03.012. [PubMed: 28372795]

Kaczka D, Dellaca RL Oscillation mechanics of the respiratory system: applications to lung disease, 2011;39(4):337–59. doi:10.1615/CritRevBiomedEng.v39.i4.60.

Kaminsky DA, Simpson SJ, Berger KI, Calverley P, de Melo PL, Dandurand R, Dellacà RL, Farah CS, Farré R, Hall GL, Ioan I, Irvin CG, Kaczka DW, King GG, Kurosawa H, Lombardi E, Maksym GN, Marchal F, Oostveen E, Oppenheimer BW, Robinson PD, van den Berge M, Thamrin C, 2022. Clinical significance and applications of oscillometry. Eur. Respir. Rev. 31 (163), 210208. 10.1183/16000617.0208-2021. [PubMed: 35140105]

King GG, Bates J, Berger KI, Calverley P, de Melo PL, Dellacà RL, Farré R, Hall GL, Ioan I, Irvin CG, Kaczka DW, Kaminsky DA, Kurosawa H, Lombardi E, Maksym GN, Marchal F, Oppenheimer BW, Simpson SJ, Thamrin C, van den Berge M, Oostveen E, 2020. Technical standards for respiratory oscillometry. Eur. Respir. J. 55 (2), 1900753. 10.1183/13993003.00753-2019. [PubMed: 31772002]

Koullapis PG, Hofemeier P, Sznitman J, Kassinos SC., 2018. An efficient computational fluid-particle dynamics method to predict deposition in a simplified approximation of the deep lung. Eur. J. Pharm. Sci. 113, 132–144. 10.1016/j.ejps.2017.09.016. Epub 2017/09/18 [PubMed: 28917963]

Koullapis PG, Stylianou FS, Sznitman J, Olsson B, Kassinos SC., 2020. Towards whole-lung simulations of aerosol deposition: a model of the deep lung. J. Aerosol. Sci. 144, 105541. 10.1016/j.jaerosci.2020.105541.

Kuprat AP, Price O, Asgharian B, Singh RK, Colby S, Yugulis K, Corley RA, Darquenne C, 2023. Automated bidirectional coupling of multiscale models of aerosol dosimetry: validation with subject-specific deposition data. J. Aerosol. Sci. 174, 106233. 10.1016/j.jaerosci.2023.106233. [PubMed: 37637507]

Li B, Christensen GE, Hoffman EA, McLennan G, Reinhardt JM., 2012. Establishing a normative atlas of the human lung: computing the average transformation and atlas construction. Acad. Radiol. 19 (11), 1368–1381. 10.1016/j.acra.2012.04.025. Epub 20120828 [PubMed: 22951110]

Lin CL, Hoffman EA, Kassinos S, Kassinos S, Bäckman P, Conway J, Hickey AJ, 2021. Chapter 14 - Machine Learning and in Silico Methods. Academic Press, pp. 375–390 editors. Inhaled Medicines.

Longest PW, Tian G, Walenga RL, Hindle M, 2012. Comparing MDI and DPI aerosol deposition using in vitro experiments and a new stochastic individual path (SIP) model of the conducting airways. Pharm. Res. 29 (6), 1670–1688. 10.1007/s11095-012-0691-y. [PubMed: 22290350]

Ma D, Cruz MJ, Ojanguren I, Romero-Mesones C, Varona-Porres D, Munoz X, 2021. Risk factors for the development of bronchiectasis in patients with asthma. Sci. Rep. 11 (1), 22820. 10.1038/s41598-021-02332-w. [PubMed: 34819607]

Manoharan A, von Wilamowitz-Moellendorff A, Morrison A, Lipworth BJ, 2016. Effects of formoterol or salmeterol on impulse oscillometry in patients with persistent asthma. J. Allergy Clin. Immunol. 137 (3). 10.1016/j.jaci.2015.06.012, 727–33.e1Epub 20150726 [PubMed: 26220533]

Matsumoto H, 2022. Bronchiectasis in severe asthma and asthmatic components in bronchiectasis. Respir. Investig. 60 (2), 187–196. 10.1016/j.resinv.2021.11.004.

Miot HA., 2018. Correlation analysis in clinical and experimental studies. J. Vasc. Bras. 17 (4), 275–279. 10.1590/1677-5449.174118. [PubMed: 30787944]

National Asthma Education and Prevention Program TEPotDaMoA, 2007. Expert Panel Report 3: Guidelines for the Diagnosis and Management of Asthma. Bethesda (MD). National Heart, Lung, and Blood Institute (US). Available from. https://www.ncbi.nlm.nih.gov/books/NBK7230/#A199.

Park SW, Park JS, Jeong SH, Lee YN, Hwangbo Y, Park JS, Lee JH, Jang AS, Kim DJ, ST Uh, Kim YH, Park C-S, 2012. Air trapping is a major determinant of persistent airway obstruction in asthmatics. Respir. Med. 106 (6), 786–793. 10.1016/j.rmed.2012.02.012. [PubMed: 22445772]

Paul AR, Khan F, Jain A, Saha SC., 2021. Deposition of smoke particles in human airways with realistic waveform. Atmosphere 12 (7), 912. 10.3390/atmos12070912 (Basel)

Porsbjerg C, Melén E, Lehtimäki L, Shaw D, 2023. Asthma. Lancet 401 (10379), 858–873. 10.1016/S0140-6736(22)02125-0. [PubMed: 36682372]

Postma DS, Dekhuijzen R, van der Molen T, Martin RJ, van Aalderen W, Roche N, Guilbert TW, Israel E, van Eickels D, Khalid JM, Herings RMC, Overbeek JA, Miglio C, Thomas V, Hutton C, Hillyer EV, Price DB., 2017. Asthma-related outcomes in patients initiating extrafine ciclesonide or fine-particle inhaled corticosteroids. Allergy Asthma Immunol. Res. 9 (2), 116–125. [PubMed: 28102056]

Rajaraman PK, Choi J, Hoffman EA, O'Shaughnessy PT, Choi S, Delvadia R, Babiskin A, Walenga R, Lin CL, 2020. Transport and deposition of hygroscopic particles in asthmatic subjects with and without airway narrowing. J. Aerosol. Sci. 146, 105581. 10.1016/j.jaerosci.2020.105581. [PubMed: 32346183]

Sadafi H, Monshi Tousi N, De Backer W, De Backer J, 2024. Validation of computational fluid dynamics models for airway deposition with SPECT data of the same population. Sci. Rep. 14 (1), 5492. 10.1038/s41598-024-56033-1. [PubMed: 38448648]

Schum M, Yeh H-C, 1980. Theoretical evaluation of aerosol deposition in anatomical models of mammalian lung airways. Bull. Math. Biol. 42 (1), 1–15. [PubMed: 7357118]

Singh D, Jain A, Paul AR, editors. Numerical Study on Particle Deposition in Healthy Human Airways and Airways with Glomus Tumor, 2020.

Smith H Human respiratory tract model for radiological protection. ICRP Publication 66. 1994.

Srivastav V, Jain A, 2011. Computational fluid dynamics study of airflow and particle transport in third to sixth generation human respiratory tract. Int. J. Emerg. Multidiscip. Fluid Sci. 3, 227–234. 10.1260/1756-8315.3.4.227.

Tawhai MH, Hoffman EA, Lin CL., 2009. The lung physiome: merging imaging-based measures with predictive computational models. Interdiscip. Rev. Syst. Biol. Med. 1 (1), 61–72. 10.1002/wsbm.17. Wiley

Tawhai MH, Clark AR, Chase JG., 2019. The Lung Physiome and virtual patient models: from morphometry to clinical translation. Morphologie 103 (343), 131–138. 10.1016/j.morpho.2019.09.003. Epub 20190927 [PubMed: 31570307]

Uppaluri R, Hoffman EA, Sonka M, Hartley PG, Hunninghake GW, McLennan G, 1999. Computer recognition of regional lung disease patterns. Am. J. Respir. Crit. Care Med. 160 (2), 648–654. 10.1164/ajrccm.160.2.9804094. [PubMed: 10430742]

Usmani OS, Singh D, Spinola M, Bizzi A, Barnes PJ., 2016. The prevalence of small airways disease in adult asthma: a systematic literature review. Respir. Med. 116, 19–27. 10.1016/j.rmed.2016.05.006. [PubMed: 27296816]

Wenzel SE, Busse WW., 2007. Severe asthma: lessons from the severe asthma research program. J. Allergy Clin. Immunol. 119 (1), 14–21. 10.1016/j.jaci.2006.10.025. [PubMed: 17208583]

Yeh HC, Schum GM., 1980. Models of human lung airways and their application to inhaled particle deposition. Bull. Math. Biol. 42 (3), 461–480. 10.1016/S0092-8240(80)80060-7. [PubMed: 7378614]

Zhang X, Li F, Rajaraman PK, Choi J, Comellas AP, Hoffman EA, Smith BM, Lin CL, 2022. A computed tomography imaging-based subject-specific whole-lung deposition model. Eur. J. Pharm. Sci. 177, 106272. 10.1016/j.ejps.2022.106272. [PubMed: 35908637]

Zhang X, Li F, Rajaraman PK, Comellas AP, Hoffman EA, Lin C-L, 2024. Investigating distributions of inhaled aerosols in the lungs of post-COVID-19 clusters through a unified imaging and modeling approach. Eur. J. Pharm. Sci. 195, 106724. 10.1016/j.ejps.2024.106724. [PubMed: 38340875]

Zinellu E, Piras B, Ruzittu GGM, Fois SS, Fois AG, Pirina P, 2019. Recent advances in inflammation and treatment of small airways in asthma. Int. J. Mol. Sci. 20 (11). 10.3390/ijms20112617. Epub 20190528

Zou C 3rd, Li F, Choi J, Haghighi B, Choi S, Rajaraman PK, Comellas AP, Newell JD, Lee CH, Barr RG, Bleecker E, Cooper CB, Couper D, Han M, Hansel NN, Kanner RE, Kazerooni EA, Kleerup EC, Martinez FJ, O'Neal W, Paine R, Rennard SI, Smith BM, Woodruff PG, Hoffman EA, Lin CL, 2021. Longitudinal imaging-based clusters in former smokers of the COPD cohort associate with clinical characteristics: the subpopulations and intermediate outcome measures in COPD study (SPIROMICS). Int. J. Chron. Obstruct. Pulmon. Dis. 16, 1477–1496. 10.2147/copd.S301466. Epub 2021/06/10 [PubMed: 34103907]

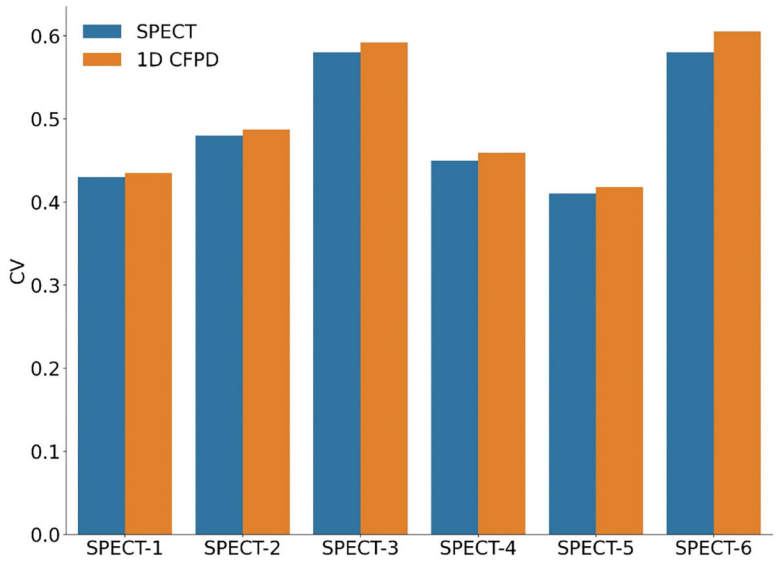

Fig. 1.

Coefficient of variation obtained from SPECT and 1D CFPD data for the 6 SPECT subjects. NRMSE < 0.05.

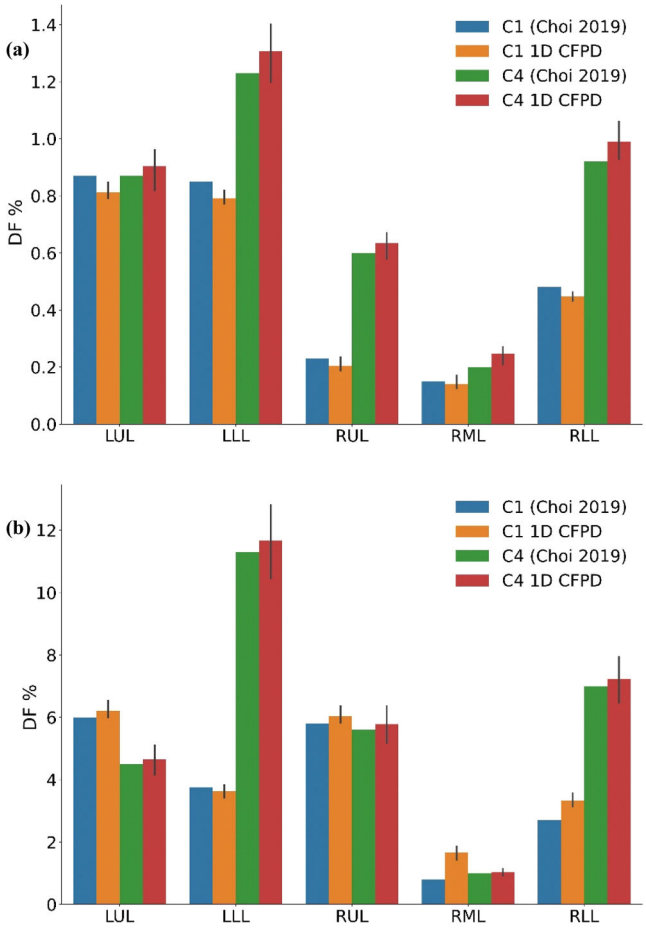

Fig. 2.

Lobar deposition fractions obtained from 1D CFPD and 3D CFPD (Choi et al., 2019) for SARP subjects with particles of (a) 1 μm and (b) 8 μm in diameter.

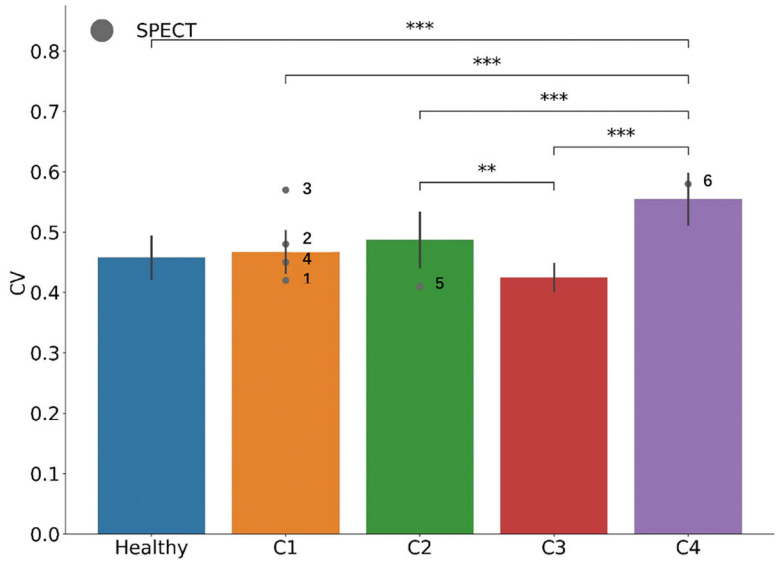

Fig. 3.

Coefficient of variation for SPECT and SARP subjects by cluster, with solid circles denoting SPECT data and bars representing SARP data. Statistical notations are: * $p < 0.05$, ** $p < 0.01$, and *** $p < 0.001$.

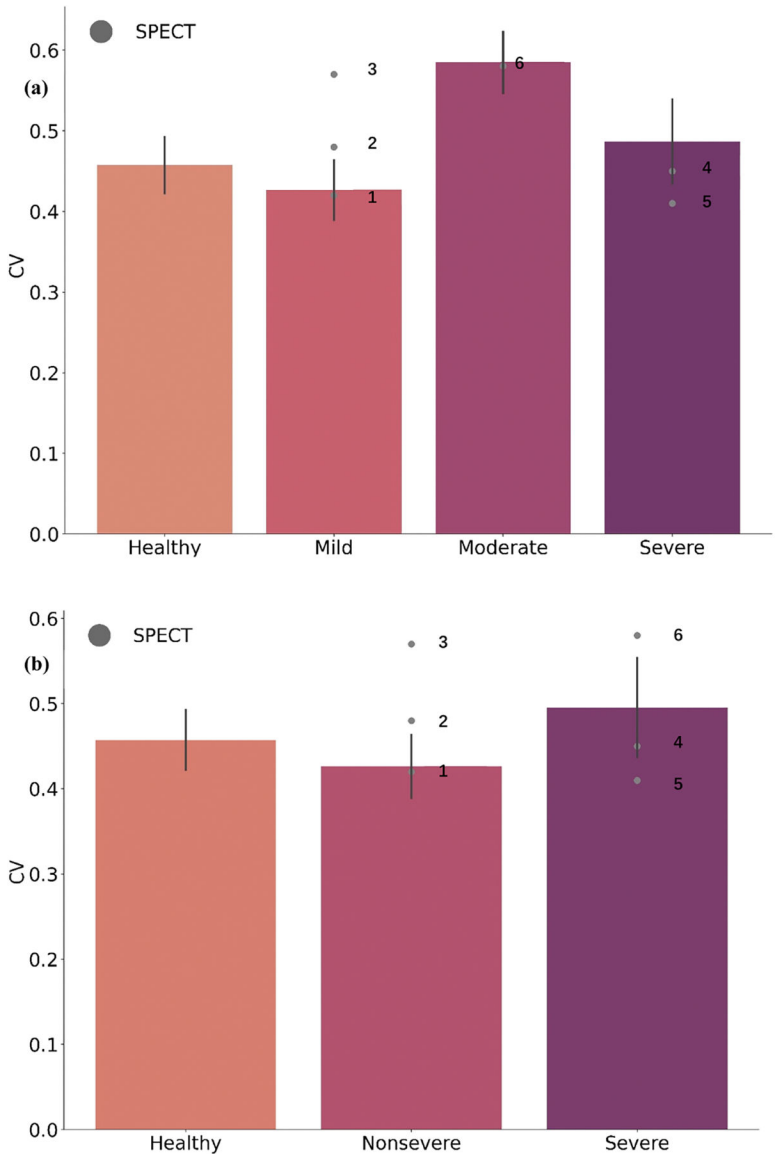

Fig. 4.

Coefficient of variation for SPECT and SARP subjects categorized by (a) NAEPP and (b) ATS guidelines, with solid circles denoting SPECT data and bars representing SARP data. There is no significant difference ($p > 0.05$) between subgroups.

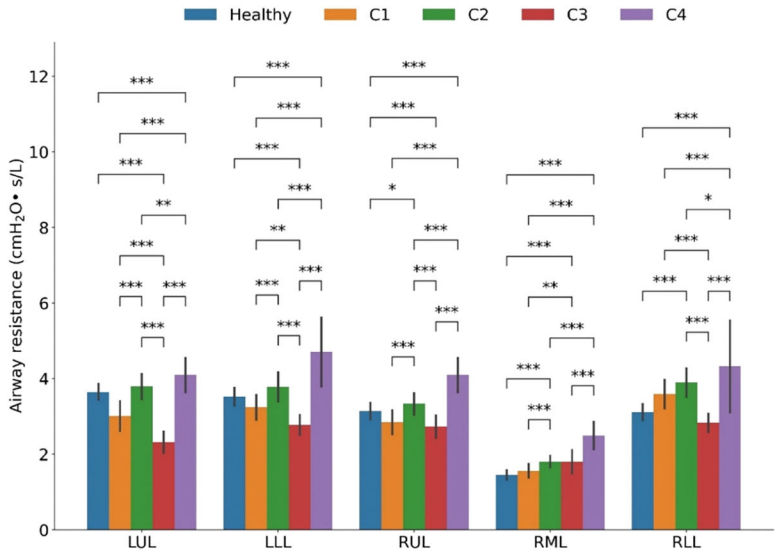

Fig. 5.

Lobar airway resistance for SARP clusters. Statistical notations are: * $p < 0.05$, ** $p < 0.01$, and *** $p < 0.001$.

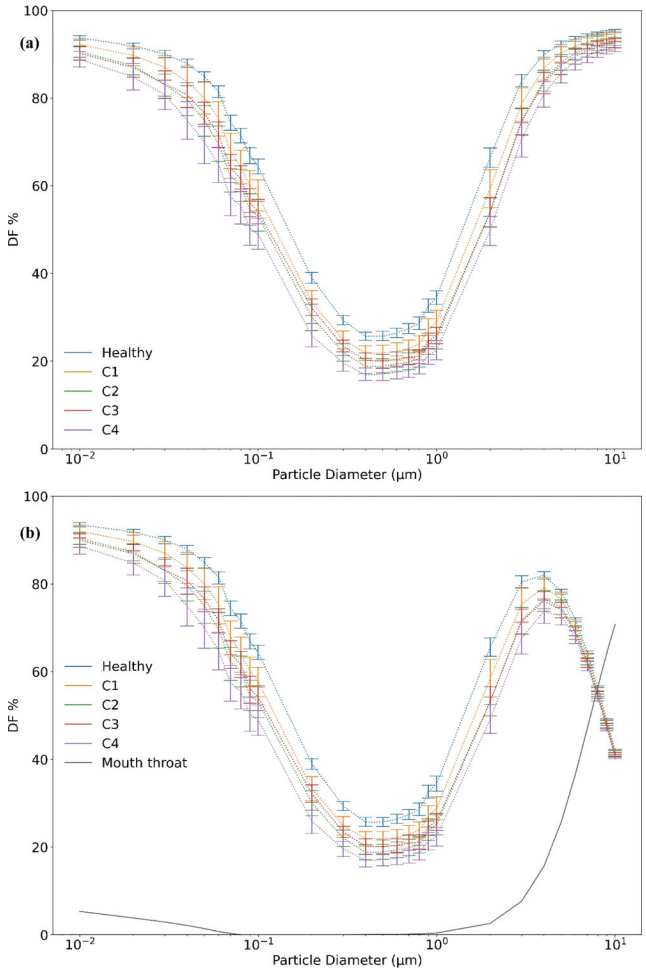

Fig. 6.

Whole lung deposition fractions for the SARP clusters during tidal breathing: (a) 1D CFPD predicted DF%, and (b) ICRP HRTM predicted $DF\%_{MT}$ and (1- $DF\%_{MT}$) × 1D CFPD predicted DF%.

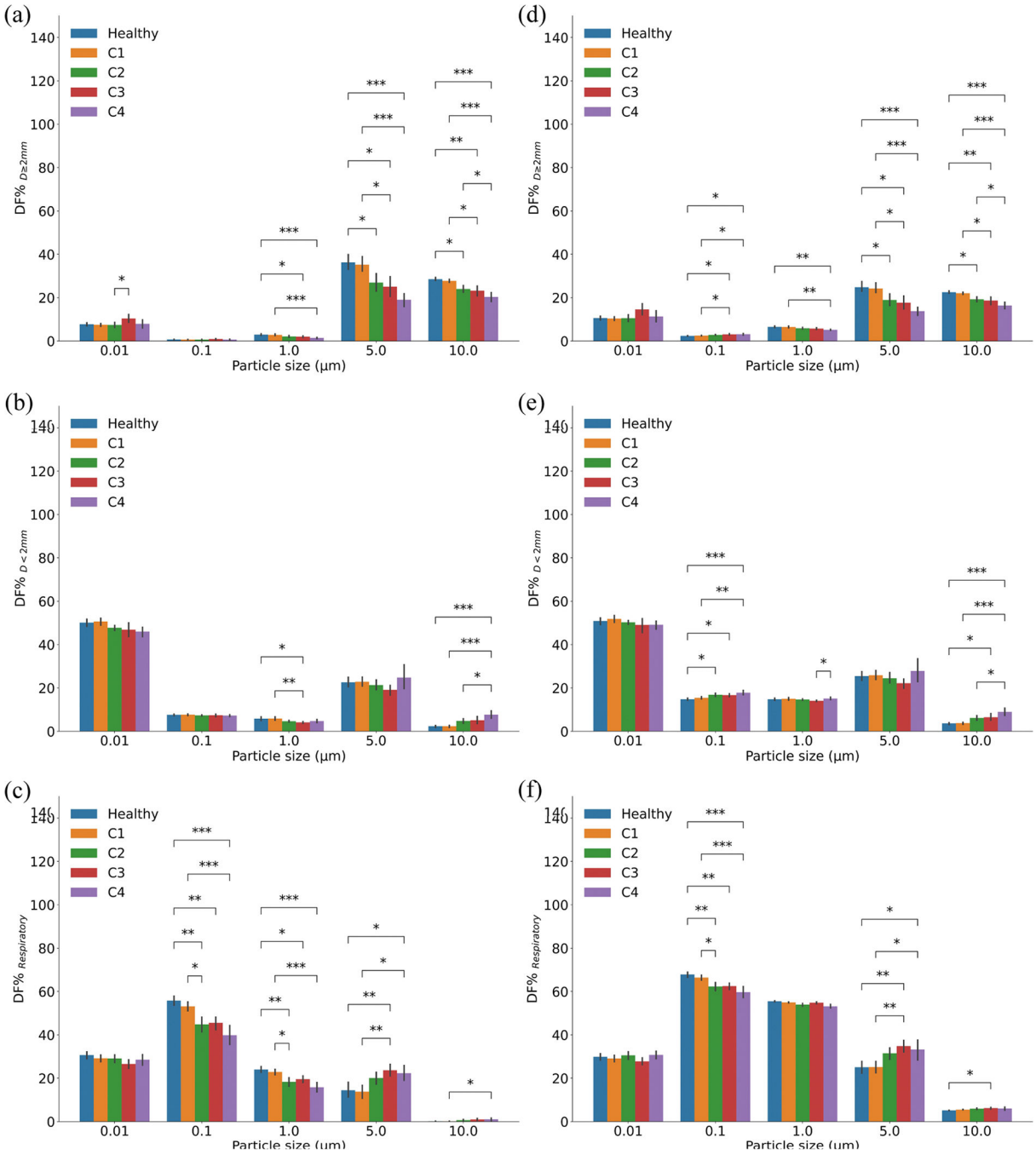

Fig. 7.

Whole-lung particle deposition fractions for SARP subjects in three regions, based on (1 - $DF\%_{MT}$) × 1D CFPD DF%. Panels (a, d) show the large conducting airway region, (b, e) the small conducting airway regions, and (c, f) the respiratory airway region. Panels (a, b, c) are for tidal breathing, and (d, e, f) for deep and slow breathing with a 10-s pause. Slow and deep form increases $DF\%_{MT}$ by 2% for 0.01 μm and 5% for 10.0 μm particles compared to tidal breathing. Statistical notations: * $p < 0.05$, ** $p < 0.01$, *** $p < 0.001$.

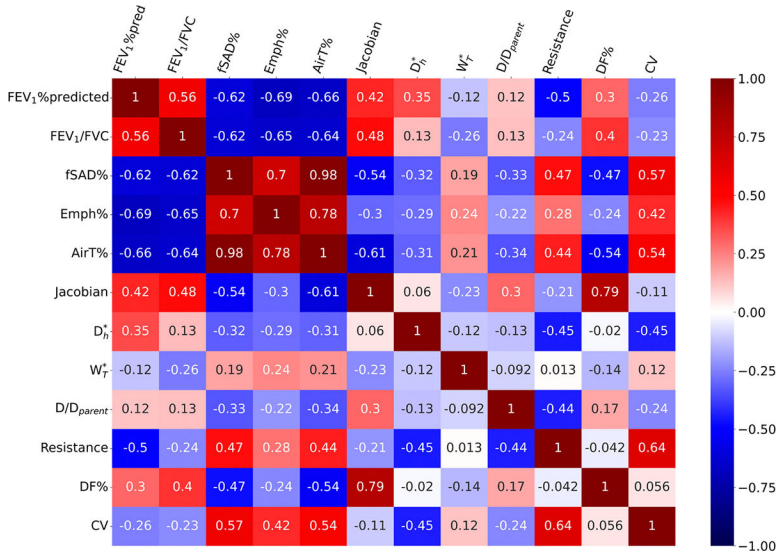

Fig. 8.

Pearson's correlation coefficients between PFT, qCT, and CFPD variables.

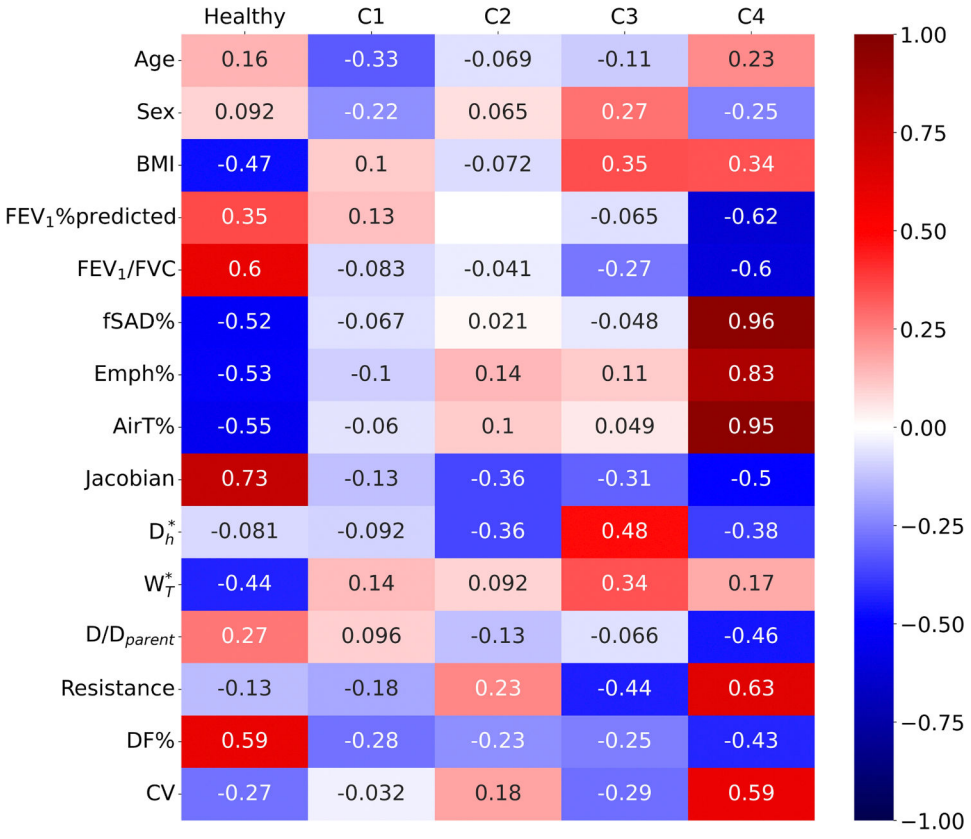

Fig. 9.

Spearman's correlation coefficients between demographic, PFT, qCT, and CFPD variables for SARP clusters.

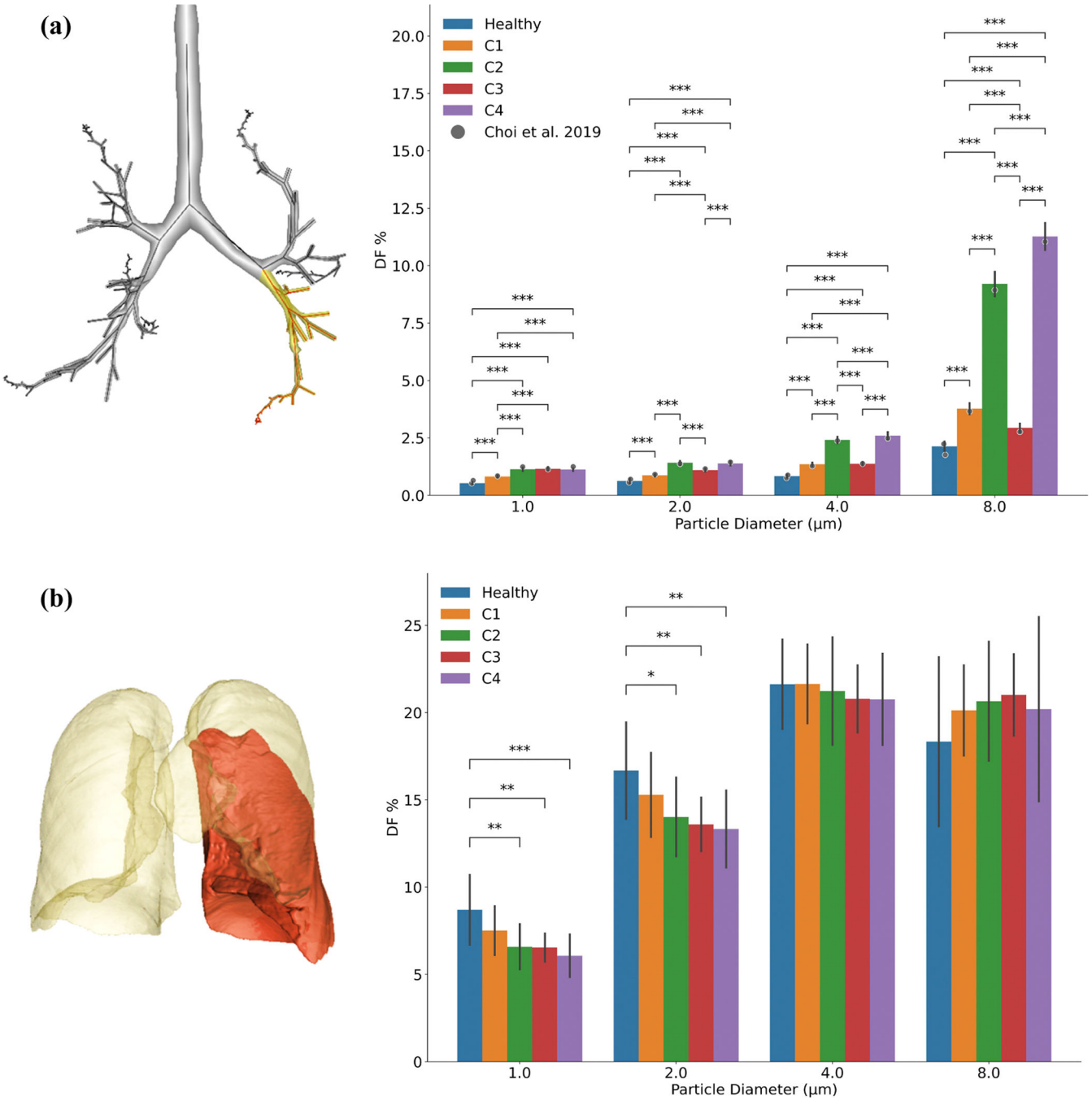

Fig. 10.

Deposition fractions in (a) the 3D path in the LLL and (b) the entire LLL among asthma clusters. Statistical notations are: * $p < 0.05$, ** $p < 0.01$, and *** $p < 0.001$.

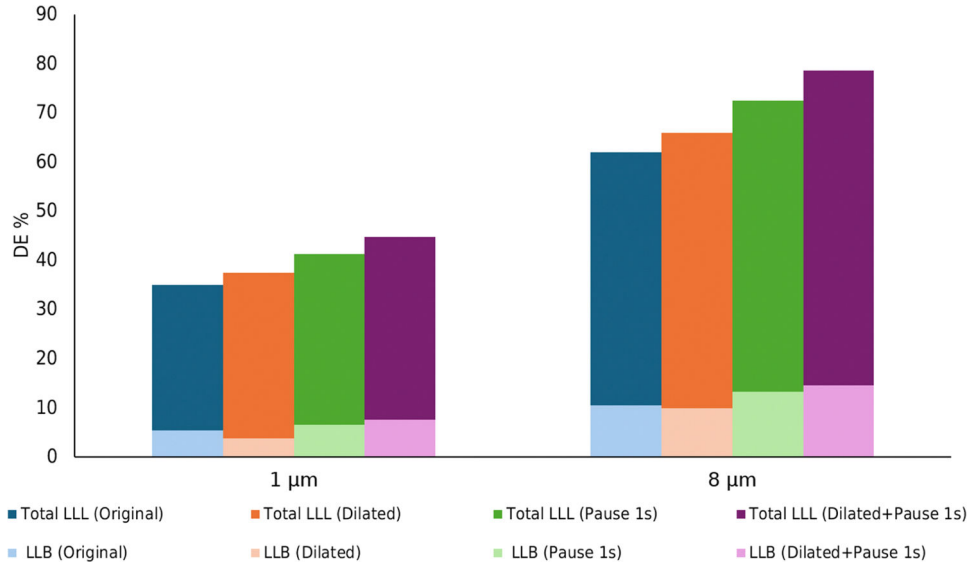

Fig. 11.

Comparison of deposition efficiencies in the LLB ($DE\%_{LLB}$) and the entire LLL ($DE\%_{LLL}$) for a C4 subject.

Table 1

Demographic and PFT data for SPECT subjects.

	SPECT-1	SPECT-2	SPECT-3	SPECT-4	SPECT-5	SPECT-6
Age (years)	21	22	21	47	72	75
Height (cm)	177	180	173	190	177	173
Weight (kg)	65.1	100.7	104.5	109.7	95.3	94.1
BMI (kg/m^2)	20.8	31.1	34.9	30.4	30.4	31.4
FEV_1 % predicted	93	83	94	50	56	63
FEV_1/FVC	81	77	82	54	57	51
TLC (L)	7.17	7.47	6.79	8	6.41	6.39
IC (L)	3.16	3.89	3.76	3.95	2.97	2.53
SC *	C1	C1	C1	C1	C2	C4
NAEPP *	Mild	Mild	Mild	Severe	Severe	Moderate
ATS *	Nonsevere	Nonsevere	Nonsevere	Severe	Severe	Severe

* Based on the qCT-based SC scheme, NAEPP guidelines, and ATS guidelines.

Table 2

Demographic and PFT data for SARP subjects ($p < 0.05$ between clusters for all variables).

Tmaging Cluster	C1 (n=76)	C2 (n=41)	C3 (n=55)	C4 (n=37)	Healthy (n=35)	*p*-value
Age (years)	31.81 (15.20)	37.22 (11.99)	44.78 (17.25)	49.38 (13.78)	42.72 (11.05)	<0.05
Height (cm)	173.26 (11.25)	171.47 (9.68)	169.57 (13.05)	173.57 (9.50)	171.44 (8.96)	<0.05
Weight (kg)	81.08 (15.82)	83.20 (22.67)	92.56 (27.12)	89.07 (17.68)	75.86 (14.12)	<0.05
BMT (kg/m^2)	26.87 (3.75)	28.36 (7.93)	31.70 (6.64)	29.40 (4.57)	25.73 (3.59)	<0.05
FEV_1 % predicted	98.24 (18.40)	86.68 (9.79)	74.37 (28.72)	56.45 (11.53)	103.81 (5.83)	<0.05
FEV_1/FVC	77.42 (7.83)	76.05 (7.37)	68.57 (15.55)	55.15 (10.17)	83.89 (13.21)	<0.05
Female (%)	52.94	52.50	65.55	47.22	51.42	<0.05
TLC (L)	5.62 (1.38)	4.19 (1.48)	4.44 (1.44)	5.10 (1.34)	5.87 (1.30)	0.07
TC (L)	3.26 (0.83)	3.51 (0.69)	2.32 (1.21)	2.63 (0.91)	2.18 (1.10)	0.09
NAEPP Mild/Moderate/Severe Asthma (%)	67.1/21.0/11.9	48.8/36.6/14.6	56.4/18.2/25.4	17.1/22.9/60.0		
ATS Severe Asthma (%)	39.5	52.5	74.5	72.9		

Values expressed as mean (SD) or number (%).

Table 3

Key qCT variables for SARP clusters and healthy controls.

	C1	C2	C3	C4	Healthy	*p*-value
Jacobian	2.46 (0.21)	1.71 (0.26)	2.00 (0.17)	1.48 (0.21)	2.90 (0.57)	<0.05
AirT%	3.15 (0.40)	8.13 (0.61)	7.22 (0.62)	24.92 (10.13)	2.21 (0.51)	<0.05
Emph%	2.98 (0.41)	3.27 (0.39)	3.08 (0.24)	6.47 (0.62)	1.09 (0.22)	<0.05
fSAD%	0.97 (0.10)	3.46 (0.37)	3.31 (0.32)	15.28 (0.76)	1.37 (0.34)	<0.05
$D^{*}_{h,\,sLLL}$	0.33 (0.04)	0.28 (0.05)	0.36 (0.06)	0.27 (0.05)	0.34 (0.07)	<0.05
$W^{*}_{T,\,sRUL}$	0.61 (0.06)	0.60 (0.06)	0.67 (0.05)	0.60 (0.05)	0.52 (0.04)	<0.05
$D^{*}_{h,BronInt}$	0.66 (0.07)	0.61 (0.05)	0.72 (0.04)	0.64 (0.03)	0.61 (0.06)	<0.05
$W^{*}_{T,BronInt}$	0.62 (0.04)	0.65 (0.06)	0.74 (0.03)	0.66 (0.05)	0.58 (0.04)	<0.05
$Vent_{RUL}$	0.17 (0.01)	0.18 (0.02)	0.20 (0.02)	0.17 (0.02)	0.17 (0.01)	<0.05
$Jacobian_{LUL}$	2.25 (0.24)	1.63 (0.27)	1.95 (0.29)	1.42 (0.20)	2.80 (0.67)	<0.05
$D^{*}_{h,RMB}$	0.87 (0.07)	0.80 (0.06)	0.88 (0.09)	0.80 (0.06)	0.85 (0.07)	<0.05
$W^{*}_{T,sRML}$	0.57 (0.06)	0.55 (0.03)	0.64 (0.05)	0.57 (0.04)	0.50 (0.30)	<0.05
ADI_{LUL}	0.49 (0.07)	0.34 (0.06)	0.42 (0.06)	0.33 (0.17)	0.57 (0.11)	<0.05
$D\ /D_{parent}$	0.83 (0.01)	0.80 (0.02)	0.83 (0.02)	0.77 (0.05)	0.83 (0.02)	<0.05
Bronchovascular %	11.79 (1.88)	12.32 (2.76)	12.50 (2.15)	12.42 (1.68)	11.79 (1.34)	<0.05

Values expressed as mean (SD) or number (%). Full names of each variable or region are described in Table S1 in the supplementary material.

Table 4

Key qCT variables for SPECT subjects.

	SPECT-1	SPECT-2	SPECT-3	SPECT-4	SPECT-5	SPECT-6	SARP-3	SARP-4	SARP-5
Jacobian	2.45	2.52	2.47	2.46	2.11	1.73	2.32	2.24	2.09
AirT%	0.95	1.41	0.98	0.92	0.50	30.10	0.88	1.04	0.55
Emph%	0.36	0.57	0.42	0.19	0.27	2.93	0.26	0.49	0.28
fSAD%	0.59	0.84	0.56	0.73	0.23	27.17	0.62	0.55	0.27
$D^{*}_{h,sLLL}$	0.34	0.35	0.28	0.34	0.28	0.28	0.28	0.32	0.27
$W^{*}_{T,sRUL}$	0.55	0.65	0.61	0.59	0.63	0.58	0.59	0.63	0.62
$D^{*}_{h,BronInt}$	0.68	0.59	0.59	0.79	0.56	0.65	0.61	0.60	0.55
$W^{*}_{T,BronInt}$	0.65	0.63	0.64	0.69	0.63	0.65	0.62	0.64	0.63
$Vent_{RUL}$	0.20	0.17	0.19	0.21	0.19	0.20	0.19	0.19	0.18
$Jacobian_{LUL}$	2.20	2.08	2.31	2.27	2.00	1.66	2.17	2.16	2.10
$W^{*}_{h,RMB}$	0.94	0.83	0.85	0.96	0.72	0.84	0.84	0.85	0.77
$W^{*}_{T,sRML}$	0.54	0.58	0.57	0.58	0.57	0.59	0.55	0.55	0.57
ADI_{LUL}	0.46	0.50	0.45	0.47	0.45	0.44	0.45	0.47	0.45
D / D_{parent}	0.83	0.82	0.83	0.81	0.80	0.78	0.81	0.81	0.80
Bronchovascular%	11.82	11.74	11.92	12.35	12.41	12.23	11.98	12.13	12.19
Cluster	C1	C1	C1	C1	C2	C4	C1	C1	C2
CV	0.43	0.48	0.56	0.45	0.41	0.58	0.54	0.44	0.42
FEV_1 (%)	102	88	93	55	51	66	96	44	53
FEV_1/FVC (%)	87	83	82	60	60	53	84	51	43
NAEPP	Mild	Mild	Mild	Severe	Severe	Moderate	Mild	Severe	Severe

Full names of each qCT variable or region are described in Table S1 in the supplementary material.